

Research Article

Three-Dimensional Aerodynamic Optimization of Single-Layer Reticulated Cylindrical Roofs Subjected to Mean Wind Loads

Bingbing San , Chen Xu , and Ye Qiu 

College of Civil and Transportation Engineering, Hohai University, Nanjing 210098, China

Correspondence should be addressed to Ye Qiu; 171304020028@hhu.edu.cn

Received 20 May 2019; Revised 25 July 2019; Accepted 5 August 2019; Published 21 August 2019

Academic Editor: Robert Černý

Copyright © 2019 Bingbing San et al. This is an open access article distributed under the Creative Commons Attribution License, which permits unrestricted use, distribution, and reproduction in any medium, provided the original work is properly cited.

This paper presents a procedure to optimize the rise-to-span ratio of single-layer reticulated cylindrical roofs to improve their aerodynamic performance, by coupling the optimization method with computational fluid dynamics (CFD) and finite element analysis (FEA). Four turbulence models (standard $k-\epsilon$, RNG $k-\epsilon$, SST $k-\omega$, and RSM) were used to predict the mean wind loads on cylindrical roofs. The simulation results were compared with wind tunnel data, and the RSM turbulence model was employed. The aim of this paper is to determine the best performing rise-to-span ratio of cylindrical roofs based on the gradient algorithm. Two objective functions were considered to minimize the highest mean suction on the roof surface and the maximum response displacement of the single-layer reticulated cylindrical shell subjected to mean wind loads. The results revealed that a cylindrical roof with a rise-to-span ratio (R/S) of 1/6.25 seems to be most effective in attenuating high suctions on the roof surface. In addition, a single-layer reticulated cylindrical shell with $R/S = 1/5.5$ gives the best performance in reducing the maximum response displacement against wind loads.

1. Introduction

Cylindrical roofs represent an arch-roof form that has widespread applications, such as gymnasiums, arenas, and hangars. Since they are often lightweight and flexible, wind loads become a significant design problem, particularly for reticulated shells and tensile membrane structures. For such structures, there is a strong dependence of their aerodynamic characteristics on the curvature of the roof. Many wind tunnel studies have been undertaken to investigate wind loads on cylindrical roofs with different rise-to-span ratios [1, 2]. Chen [3] carried out surface pressure measurements on low-rise building models with various roof types in a wind tunnel. Mean pressures on cylindrical roofs were observed to decrease when the rise-to-span ratio (R/S) was ranging from 1/2 to 1/16. However, peak pressures at roof corners increased remarkably when $R/S \leq 1/8$. Chen and Yang [4] experimentally studied wind pressure characteristics of cylindrical roofs with $R/S = 1/4$ and $1/8$. Their work reported that the mean wind force coefficient of high rise-to-span ratio roof was larger than that of low R/S

case for the wind direction from 0° to 90° . Several experimental studies of wind loads on cylindrical roofs with $R/S = 1/2.5$, $1/3$, and $1/5$ have also been conducted [5–7]. A comparison of previous results indicated that windward pressures and corresponding regions were significantly reduced with a decrease in the rise-to-span ratio.

Alternatively, computational fluid dynamics simulation has been utilized as a cheaper and flexible tool for the wind load estimation, without the need to perform time-consuming wind tunnel experiments. Numerically obtained wind pressure coefficients for various arch-roof structures, as well as numerical simulation of airflow field, showed a satisfactory agreement with wind tunnels or full-scale measurements [8–10]. Moreover, CFD simulations of wind loads on cylindrical roofs with different rise-to-span ratios have shown good agreement with experimental data [11, 12].

Since aerodynamic behavior of civil structures primarily depends on their external shapes, the responses subjected to wind loads can effectively be reduced by finding the optimal shape. The search for the best performing shape through an automatic CFD-based optimization procedure is more

thorough and less time-consuming than the traditional “cut and try” approach based on wind tunnel tests. Moonoghi and Kargarmoakhar [13] presented a comprehensive review on the aerodynamic shape optimization methods developed for reducing wind loads on civil structures. Ogawa et al. [14] used a variable complexity model (VCM) with the response surface method to obtain the optimal shape of a 2-D cylindrical shell roof, in order to minimize the deformation under strong wind. Yamashita et al. [15] also applied this technique to optimize the shape of a long-span free-form shell to minimize the maximum vertical response displacement. They pointed out that the optimal shape has a uniform curvature and is close to cylindrical roof. More recently, Bernardini et al. [16] and Elshaer et al. [17] carried out tall building corner aerodynamic optimization studies by using surrogate-based approach (the Kriging model and artificial neural network model) and CFD technique to determine the optimal shape focusing on lift and drag coefficient minimization.

Despite the design of arch-roof shape is always determined by architects, it is important to give some design suggestions concerning the optimal shapes in view of aerodynamic or mechanical properties. To the authors’ knowledge, none or little effort has been dedicated to the shape optimization study of three-dimensional cylindrical roofs. It is well known that the implementation of aerodynamic shape optimization based on CFD simulations is essentially difficult for civil structures due to the bluff-body nature, the complex flow field pattern, the effects of the Reynolds number, and the presence of turbulent boundary layer in which the structures are immersed.

The main purpose of this study is to propose a CFD-based aerodynamic optimization technique to optimize the rise-to-span ratio of three-dimensional cylindrical roofs, which aims at improving their aerodynamic behavior. In this paper, firstly, the wind pressure distributions on cylindrical roofs with R/S ranging from 1/6 to 1/2 were studied by means of wind tunnel experiments and numerical simulations. The CFD simulations had been performed by a Reynolds-averaged Navier–Stokes (RANS) model using four turbulence closure models (standard $k-\epsilon$, RNG $k-\epsilon$, SST $k-\omega$, and RSM), and the numerical results were evaluated by experimental data. Secondly, considering the aerodynamic and mechanical behaviors, two optimization application examples focusing on minimizing the highest mean suction and the maximum response displacement of a single-layer reticulated cylindrical shell subjected to mean wind loads were presented, respectively. It is shown that the optimal rise-to-span ratio can be obtained successively by using the gradient algorithm, which had also been verified by comparison with the near optimal solutions.

2. Experimental Apparatus and Methods

The experiments were performed in a closed-return type wind tunnel with a test section of $4W \times 3H \times 25L$ (m^3), in the Harbin Institute of Technology. Three cylindrical roof models with rise-to-span ratios of 1/6, 1/3, and 1/2 were used in this investigation. They all have the same span $S = 0.6$ m, length $L = 0.6$ m, and wall height $h = 0.06$ m. In this study, we

considered a cylindrical roof with a span of 60 m as a prototype, which corresponds to a length scale of 1:100. A 20 mm thick base plate elevated from floor was used to reduce the boundary layer developed over the tunnel floor. The plate had 4.8 m (length) \times 2.4 m (width) dimensions, and a sharp leading edge of angle 30° . The roof model was located 0.5 m downstream from the leading edge of the base plate. The wind tunnel setups are shown in Figure 1. Characteristics of the flat-plate turbulent boundary layer were measured using a hot wire anemometer. The wind direction in this study was set normal to the ridge of roofs. The mean velocity and turbulence intensity profiles measured at model center are shown in Figure 2.

A Reynolds number sensitivity test had been conducted beforehand to check the influence of the Reynolds number on the mean wind loads on cylindrical roofs with various rise-to-span ratios. Figure 3 shows the lift and drag force coefficients for cylindrical roofs with $R/S = 1/6, 1/3,$ and $1/2$, with an Re ranging from 6.90×10^4 to 8.28×10^5 . It can be observed that the force coefficients for the roof model with $R/S = 1/6$ were nearly constant in the studied Re range. However, for cylindrical roofs with $R/S = 1/3$ and $1/2$, C_l and C_d become nearly independent of the Reynolds number when $Re > 2.48 \times 10^5$ and 4.14×10^5 , respectively. The results also reveal that a decrease in the rise-to-span ratio has caused a premature transition of the separated shear layer from laminar to turbulent. Thus, the free-stream velocity in present CFD simulations and aerodynamic optimization was fixed at $U = 20$ m/s and the corresponding Reynolds number based on the roof span was $Re = 8.28 \times 10^5$.

In this study, the effect of model scale was taken into account purely using the Strouhal number similarity, ignoring the effects of the Reynolds number and the Mach number. By equating the model and full-scale Strouhal numbers (defined as $S_t = D/T_s U$, where T_s is the vortex shedding period and D is a characteristic length of the body), it is obvious that the time scale between the model and full-scale conditions depends only on the length scale and the scale of free-stream velocity. A velocity scale of 1:2 was adopted in the present experiment (the free-stream velocity in full scale is 40 m/s), resulting in a time scale of 1:50. The sampling frequency was 625 Hz, and the wind tunnel measurement duration was 100 s, corresponding to about 1.5 hours full scale. 241 pressure taps were uniformly distributed on the roof surface, and the angle between two neighboring taps on the middle transverse cross section was 9 degrees. The maximum blockage ratio (defined as the ratio of the projected roof area to the cross-sectional area of the wind tunnel) of the tests was 1.8% for the semicylindrical roof. Surface pressures are normalized by the mean dynamic pressure $0.5 \rho U^2$ measured at the height $z = 0.36$ m. The pressure coefficient C_p can be expressed as

$$C_p = \frac{\overline{\Delta p}}{0.5 \rho U^2}, \quad (1)$$

where Δp is the instantaneous pressure difference between the surface pressure and the reference static pressure in the wind tunnel and ρ is the air density.

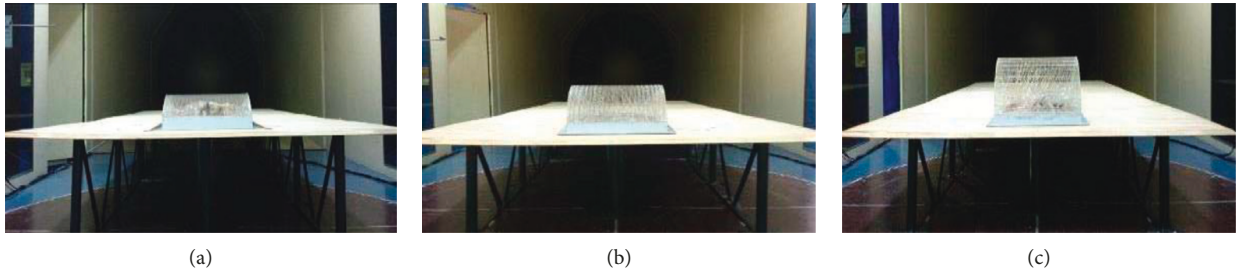


FIGURE 1: Experimental roof models. (a) $R/S = 1/6$. (b) $R/S = 1/3$. (c) $R/S = 1/2$.

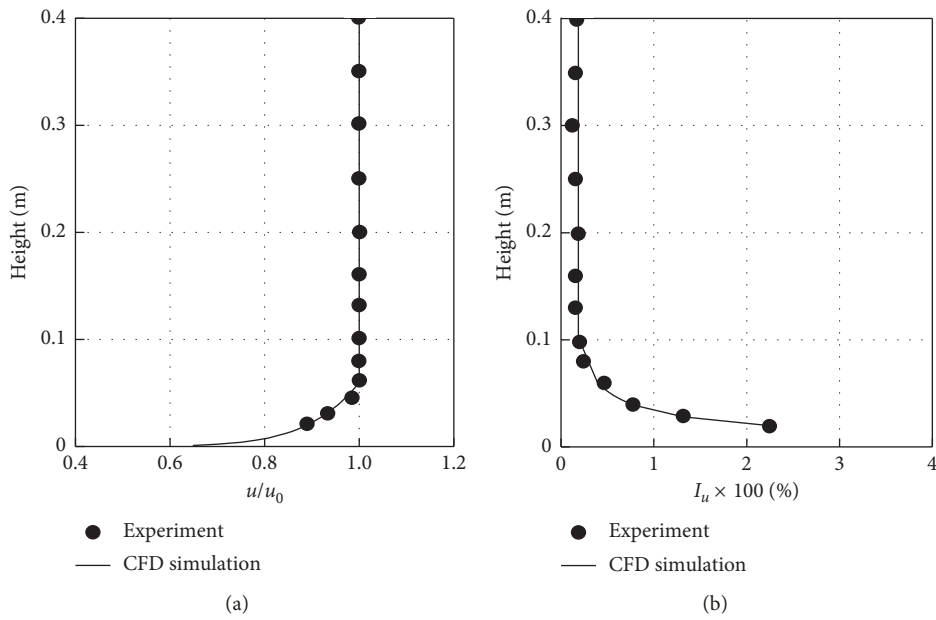


FIGURE 2: (a) Mean streamwise velocity and (b) turbulence intensity profiles measured at the model center.

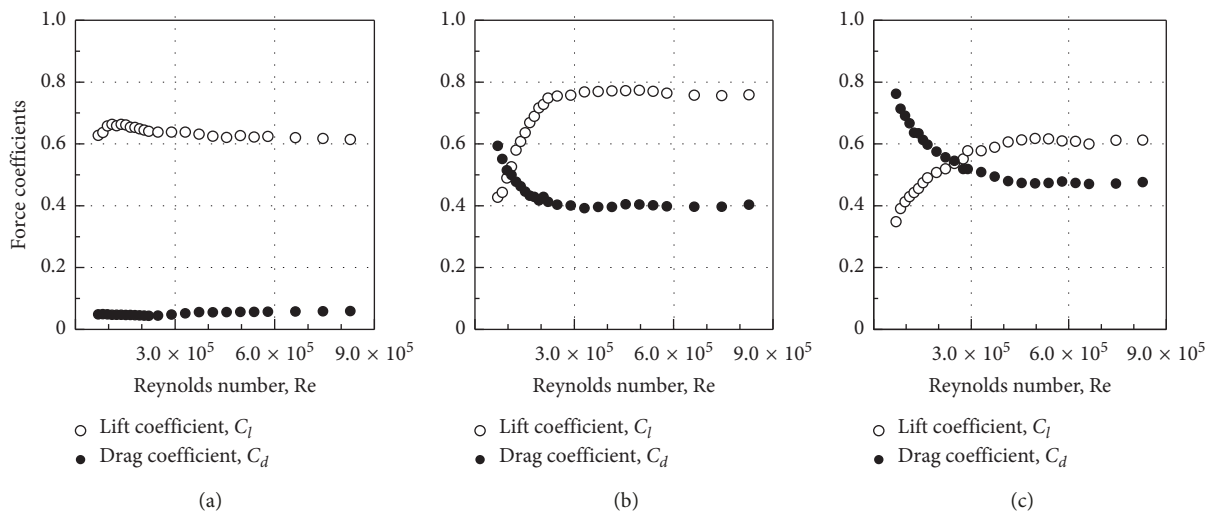


FIGURE 3: Variations of force coefficients with Reynolds number for cylindrical roofs with various rise-to-span ratios. (a) $R/S = 1/6$. (b) $R/S = 1/3$. (c) $R/S = 1/2$.

3. Numerical Methods

3.1. Governing Equations. Commercial CFD software, ANSYS Fluent 15.0, was used to simulate mean wind loads on cylindrical roofs. Airflow is assumed to be incompressible, steady, viscous, and isothermal. The time-averaged continuity and the Reynolds-averaged Navier–Stokes (RANS) momentum equations are as follows:

$$\begin{aligned} \frac{\partial u_i}{\partial x_i} &= 0, \\ \frac{\partial u_i}{\partial t} + u_j \frac{\partial u_i}{\partial x_j} &= -\frac{1}{\rho} \frac{\partial p}{\partial x_i} + \frac{\partial}{\partial x_j} \left(\nu \frac{\partial u_i}{\partial x_j} - \overline{u_i' u_j'} \right), \end{aligned} \quad (2)$$

where u_i is the i th component of velocity, x_i is the i th coordinate, t is the time, and ν is the fluid kinematic viscosity. $-\overline{u_i' u_j'}$ is the Reynolds stress generated by turbulence [18]. All the simulations were based on RANS equations using four turbulence closure models (standard k - ε , RNG k - ε , SST k - ω , and RSM) [19–22]. Details on these turbulence models are provided in the ANSYS Fluent 15.0 User's Guide [23].

3.2. Numerical Validation. In order to assess the reliability of the numerical approach for the optimization study, wind loads acting on the roof surface were simulated and compared with wind tunnel data. After some trials to check the influence of the ratio of the physical model on domain size, the final domain dimension with 16S (length) \times 9S (width) \times 5S (height) was determined, where $S = 0.6$ m is the roof span, leading a maximum blockage ratio around 1.3%. The roof model was located at 4S from the inlet boundary. Figure 4 shows the computational domain and the mesh arrangement for the roof model with $R/S = 1/2$. In order to accurately resolve the high-gradient regions of the flow field, adaptive prism grids with 6 layers were generated surrounding the roof and wall surfaces, while adaptive Cartesian grids (tetrahedral grids) were produced to fill the rest of the flow field. The first-layer prism size near the roof was $S/120$, and the span wise grid size was $S/80$, whilst the expansion ratio in the prism grid system did not exceed 1.2. The estimated values of y^+ on the roof surface were between 30 and 70. The domain was finally discretized into about 200 million grid cells after a few grid independency tests. A similar grid arrangement was employed for other roof models, with a finer resolution around the roof and wall surfaces to improve the accuracy of the simulations.

The wind tunnel inflow velocity profile as shown in Figure 2 was fitted to an exponential profile ($u(z) = u_0(z/z_0)^\alpha$) by using the RSM turbulence model, where α is the power law index ($\alpha = 0.11$) and u_0 and z_0 are the reference velocity and height ($u_0 = 20$ m/s and $z_0 = 0.06$ m), respectively. The turbulent kinetic energy and its dissipation rate at the inlet boundary can be calculated by using the following equations:

$$\begin{aligned} k_{\text{in}} &= \frac{3}{2} (u I_u)^2, \\ \varepsilon_{\text{in}} &= \left(\frac{C_\mu^{3/4} k_{\text{in}}^{3/2}}{\kappa z} \right), \end{aligned} \quad (3)$$

where κ is the von Kármán constant ($\kappa = 0.4$) and I_u is the turbulence intensity and varies from 2.3% to 0.2% in the region of the roof heights.

At ground and roof surface, standard wall functions and no slip condition had been used. Free slip conditions were considered for the side and top boundaries. At the outlet boundary, the flow had been considered fully developed. A collocated grid system by the finite volume method was used to solve the governing equations. Discretized equations have been solved by the segregated method. The semi-implicit method for pressure-linked equations (SIMPLE) was employed to solve the pressure-velocity coupling. The simulations were considered converged when the residual values dropped below 10^{-5} .

Figure 5 presents the mean pressure distributions on the middle transverse cross section of the roof obtained from wind tunnel measurements and numerical simulations. In general, the agreement of the RSM turbulence model with experimental data is acceptable, although slight differences can be observed in the wake region for the roof model with $R/S = 1/2$. The performance of any of standard k - ε and RNG k - ε turbulence models against the experimental data is not particularly good. They underestimate wind suctions over the roof apex in the case of $R/S = 1/3$ (Figure 5(b)) and overestimate $|C_p|$ values in the leeward region in the case of $R/S = 1/2$ (Figure 5(c)). SST k - ω results are worse than other turbulence models. Thus, RSM turbulence model was employed in the following aerodynamic optimization process. It should be noted that the approaching flow may separate at the leading edge of the roof with a very low rise-to-span ratio, which is not considered in the current wind tunnel tests. Accordingly, the above turbulence models cannot be validated near the roof leading edge, and the simulation results obtained there should be checked carefully.

4. Optimization Methods

4.1. Optimization Model. The aerodynamic optimization problem involves objective functions, design variables, a flow solver, and an optimization algorithm. In this study, the rise-to-span ratio was chosen as the design variable, which can significantly improve the aerodynamic performance of cylindrical roofs. Thus, the present aerodynamic optimization problem can be defined as follows:

$$\begin{cases} \text{minimize:} & F\left(\frac{R}{S}\right), \\ \text{subject to:} & l_{\text{limit}} \leq \frac{R}{S} \leq u_{\text{limit}}, \end{cases} \quad (4)$$

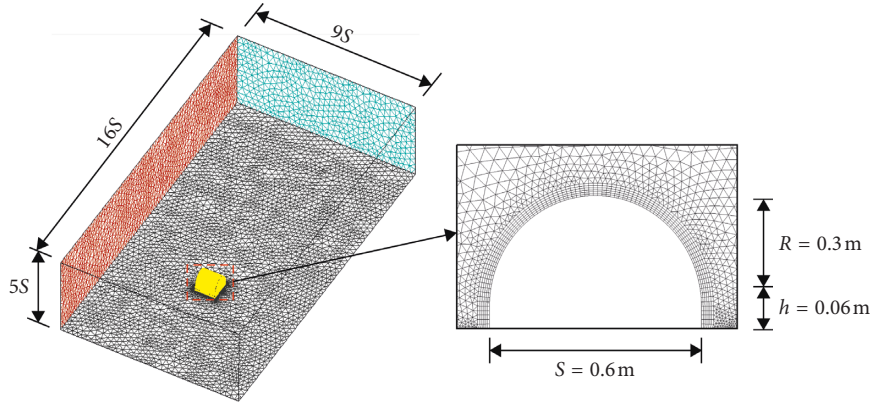


FIGURE 4: Computational domain and grid system used in this study.

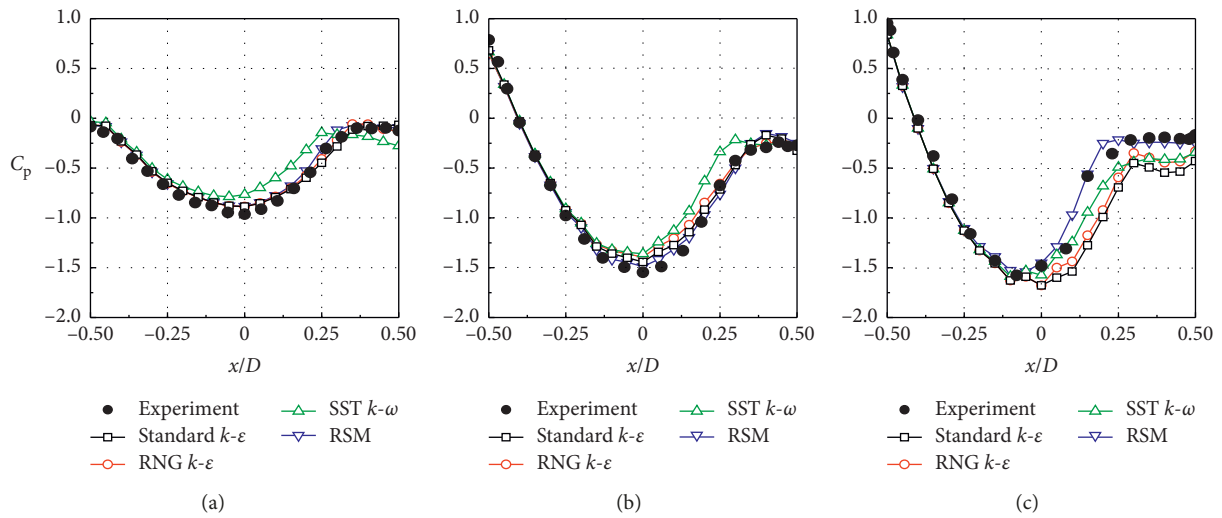


FIGURE 5: Experimental and numerical mean pressure distributions on the middle transverse cross sections of the cylindrical roof. (a) $R/S = 1/6$. (b) $R/S = 1/3$. (c) $R/S = 1/2$.

where $F(R/S)$ is the objective function, R/S is the design variable, and l_{limit} and u_{limit} are the lower and upper limits of the design variable, respectively.

Different optimization goals allow the designer to explore more alternatives for the design of the cylindrical roof, with aerodynamic or mechanical considerations. Large wind suction may occur near the leading edge of windward roof and roof apex under strong wind, which are critical for the design of roof cladding and its fixings. Thus, the first objective is to minimize the highest mean suction on the roof surface, and the objective function $F_1(R/S)$ is defined as

$$\text{minimize: } F_1\left(\frac{R}{S}\right) = \max\{|C_{pi}|\}, \quad (5)$$

where C_{pi} denotes the mean pressure coefficient of the i th node.

It is important to consider the wind-induced response for designing a lightweight spatial structure because of the lack in out-of-plane stiffness. As a result, the second objective is to minimize the maximum response displacement under mean wind loads, and the objective function $F_2(R/S)$ is given as

$$\text{minimize: } F_2\left(\frac{R}{S}\right) = \max\{|w_i|\}, \quad (6)$$

where w_i denotes the response displacement value of the i th node. The response displacements of reticulated cylindrical shells against mean wind loads were obtained by using the finite element analysis.

4.2. Optimization Algorithm. The aerodynamic optimization problem in this study can be treated as a single-objective optimization problem, and the gradient algorithm was used. In case of single-objective optimization problems with low number of design variables, gradient-based methods are more suitable than nongradient-based methods since they are in general computationally faster. However, their main drawback is that they may converge to local minima, and the convergence to global minima mainly depends on the initial variable chosen by the user. The basic idea of gradient algorithm is that the objective function reaches its minimum or maximum in its gradient direction. The iterative algorithm of the gradient algorithm using design variable R/S can be expressed as

$$\left(\frac{R}{S}\right)^{(i+j)} = \left(\frac{R}{S}\right)^{(i)} + \alpha_i \cdot d^{(i)}, \quad (7)$$

where i is the iteration step, α_i is the search step size calculated by the golden section search method, and $d^{(i)}$ is the negative gradient value and is calculated as $d^{(i)} = -\nabla^{(i)} F(R/S) = -\partial F(R/S)/\partial (R/S)$. More details on the gradient algorithm are provided in the literature [24–26]. The convergence tolerance τ is defined as

$$\tau = \left| F^{(i+1)}\left(\frac{R}{S}\right) - F^{(i)}\left(\frac{R}{S}\right) \right|. \quad (8)$$

The optimization procedure will stop when $\tau \leq 10^{-4}$.

The aerodynamic optimization procedure in this study can be summarized as a flow chart shown in Figure 6, which was implemented by using a FORTRAN program. There are five steps in applying this program: (1) assign the initial design variable $(R/S)^{(i)}$ and set $i = 0$; (2) carry out 3D CFD simulations or FEA analysis at $(R/S)^{(i)}$ to calculate the objective function $F^{(i)}(R/S)$; (3) let $i \rightarrow i + 1$ and update the design variable $(R/S)^{(i+1)}$ by the steepest decent algorithm; (4) calculate the new objective function $F^{(i+1)}(R/S)$ based on the CFD or FEA analysis; (5) check the convergence criterion; if it is not satisfied, go to steps (3) and (4) until the optimal solution is obtained.

5. Results and Discussion

5.1. Effect of Rise-to-Span Ratio. It is well known that the rise-to-span ratio casts significant influence on the characteristics of wind loads on cylindrical roofs. At the very beginning of this investigation, the mean pressure distribution and its effects on single-layer reticulated cylindrical shells considering different rise-to-span ratios, which have widely been used in practice, were investigated. The contours of mean pressure coefficients on cylindrical roofs with $R/S = 1/6$, $1/3$, and $1/2$ are shown in Figure 7. Computed mean pressure distributions for the three roof models are, in general, in good agreement with the experimental data. It should be noted that some deviation exists between the measured and numerical results mainly due to the limited number of pressure taps installed on the roof models. It is observed from Figure 7 that the overall pressure distributions exhibit a nearly 2-dimensional pattern, except for the near-edge regions where a 3-dimensional effect may be significant. Most of the area of the roofs with $R/S = 1/3$ and $1/2$ are dominated by wind suctions except for a small region near the leading edge of windward surface with positive pressures. However, only negative pressures are observed for the roof model with $R/S = 1/6$. In addition, the highest mean suction occurs near the roof apex and increases remarkably with the rise-to-span ratio.

In this study, a rigidly jointed single-layer reticulated cylindrical shell was chosen as the analysis model, without considering the interaction between the aerodynamic force and the displacement of the roof surface. According to the geometric scale of $1/100$ in the wind tunnel, the span of the cylindrical shell was 60 m. Figure 8 shows a single-layered

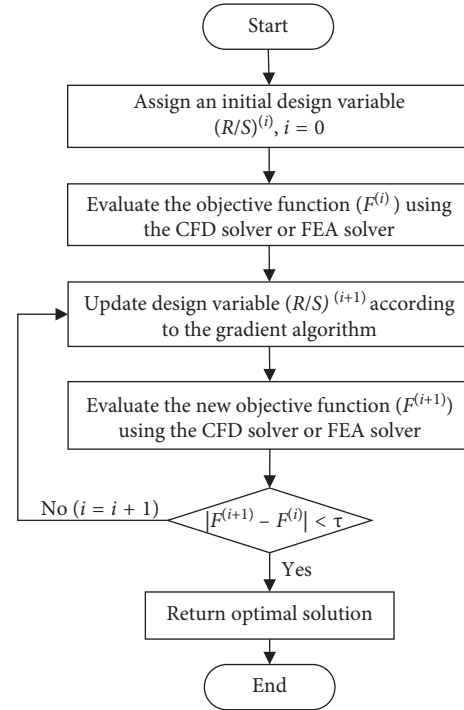


FIGURE 6: Flow chart of the aerodynamic optimization procedure.

Kiewitt-6 reticulated cylindrical shell with $R/S = 1/2$. The division number N_{div} of reticulated cylindrical shells under different R/S conditions in the span wise direction was fixed at 21. The shell model was constructed of steel pipes with dimensions of 140 mm diameter and 6 mm thickness ($\phi 140 \times 6$ mm). All the joints on the boundary were assumed to be hinged on the rigid wall. It should be noted that wind load effects on cylindrical shells mainly depend on the special mechanical properties of this structural type. Just analysis models with a length-to-span ratio $L/S = 1.0$ were considered in the current work. For other roof models with different L/S , the basic wind effects are always the same [6].

Figure 9 compares the response displacements of single-layer reticulated cylindrical shells against mean wind loads obtained from numerical and experimental results. The general agreement between wind tunnel and numerical results is quite good. From the results in Figure 9, it is found that the rise-to-span ratio has a significant effect on the maximum response displacement, ranging from 0.006 m to 0.011 m. It is interesting to observe that the maximum response displacement $|w|_{max}$ of cylindrical shells with $R/S = 1/6$ and $1/2$ occurs near the roof apex, while $|w|_{max}$ is found in the windward region of the roof in the case of $R/S = 1/3$.

In order to gain understanding on the effects of the rise-to-span ratio on the wind loads and wind-induced behaviors of cylindrical roofs, we have extended the CFD calculations discussed above. Figure 10 shows variations of the highest mean suction ($|C_p|_{max}$) and the maximum response displacement ($|w|_{max}$) among all surface nodes with different rise-to-span ratios (R/S), where R/S ranges from $1/10$ to $1/2$. Since the strong advantage of CFD is that detailed flow field

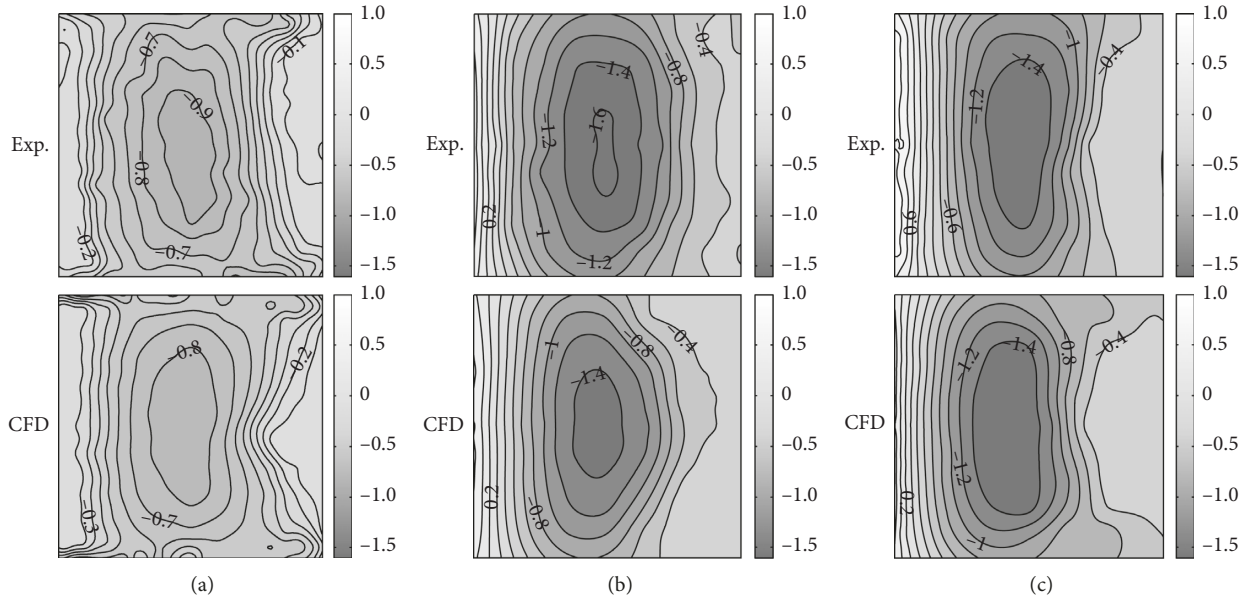


FIGURE 7: Numerical results of contours of mean pressure coefficients on cylindrical roofs in comparison with experimental results. (a) $R/S = 1/6$. (b) $R/S = 1/3$. (c) $R/S = 1/2$.

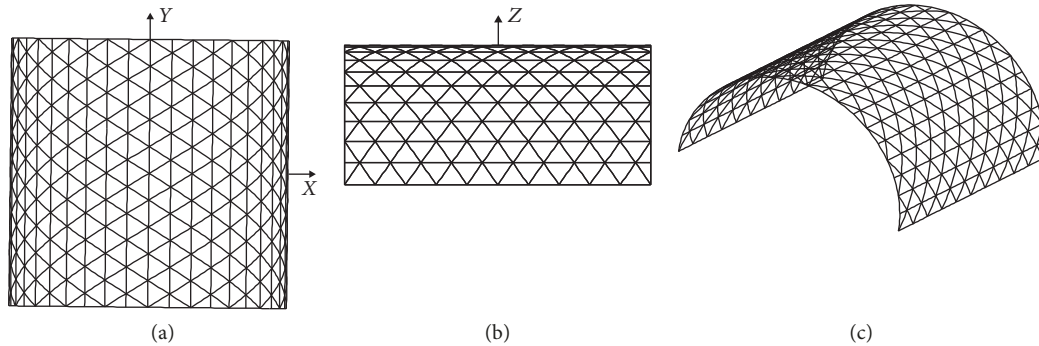


FIGURE 8: Analysis model: a single-layer reticulated cylindrical shell. (a) Top view. (b) Lateral view. (c) 3D view.

information can be easily obtained, Figure 11 shows the streamline contours around cylindrical roofs under different rise-to-span ratio conditions. As shown in Figure 10(a), for $R/S < 1/6$, the highest mean suction decreases with an increase in the rise-to-span ratio, and it increases gradually thereafter. It should be noted that relatively large suction ($|C_{p}|_{\max} > 1.7$) can be observed for roof models with $R/S = 1/10$ and $1/8$ due to the separation of approaching flow at the leading edge of the roof, as shown in Figures 11(a) and 11(b). Furthermore, large suction occurs only at the roof apex for roof models with a large rise-to-span ratio ($R/S \geq 1/6$), and no flow separation can be observed at the leading edge, as presented in Figures 11(d)–11(h).

It can be seen from Figure 10(b) that the maximum response displacement of a single-layer reticulated cylindrical shell decreases obviously with R/S up to $1/5$ and then increases thereafter. In conclusion, it is of interest to note that a cylindrical roof with R/S ranging between $1/7$ and $1/5$ shows a relatively good aerodynamic or mechanical performance, and the optimal R/S value will be determined through the proposed optimization procedure.

5.2. Optimal Design of Single-Layer Reticulated Cylindrical Roofs. The goal of current aerodynamic optimization is to efficiently and accurately determine an optimal rise-to-span ratio that attains the best aerodynamic or mechanical performance of cylindrical roofs. Accordingly, two objective functions were employed to minimize the highest mean suction on the roof surface and the maximum response displacement of a single-layer reticulated cylindrical shell. The gradient algorithm was used to solve this optimization problem. The main drawback of this method is that it might converge to local minima. Thus, two initial rise-to-span ratios $(R/S)^{(0)} = 1/10$ and $1/2$, which correspond to the lower and upper limits of the design variable respectively, were used simultaneously to find the global minima. The optimization procedure was constructed for the above two optimization problems until the optimal solutions are obtained (convergence tolerance $\tau < 10^{-4}$).

5.2.1. Highest Mean Suction Optimization. The optimal results reveal that a cylindrical roof with $R/S = 1/6.25$

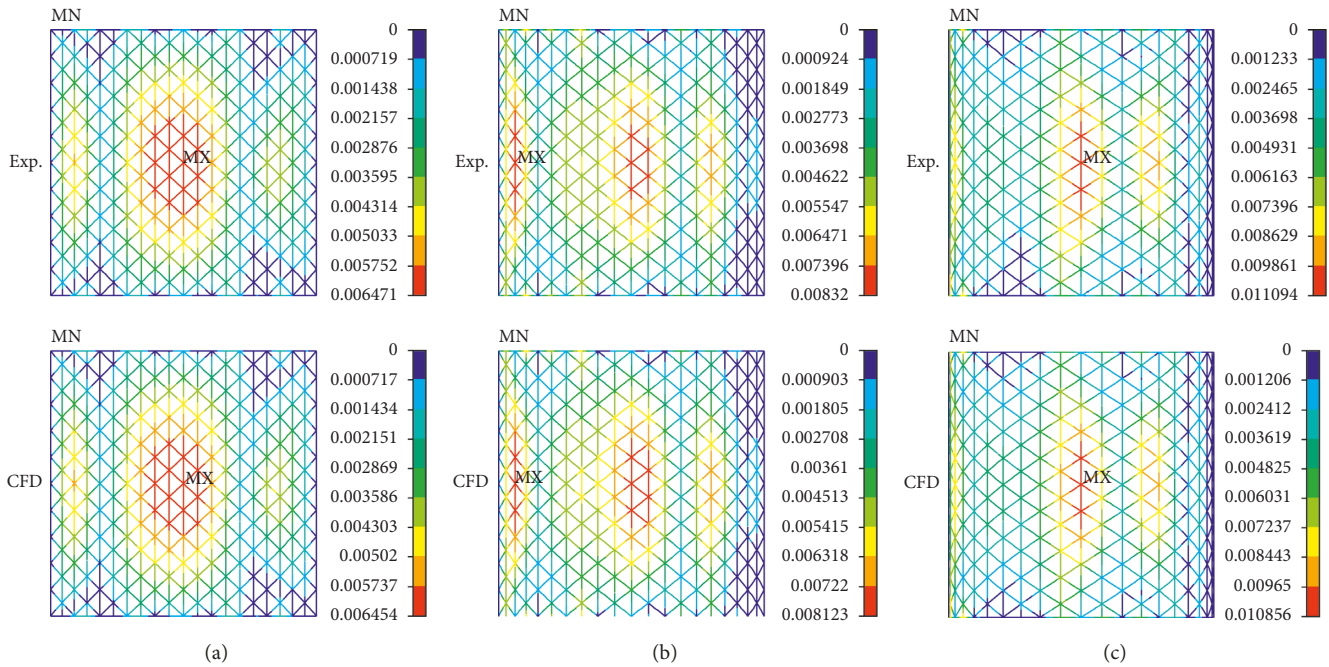


FIGURE 9: Comparison of the response displacements of cylindrical shells against wind loads obtained from numerical and experimental results. (a) $R/S = 1/6$. (b) $R/S = 1/3$. (c) $R/S = 1/2$.

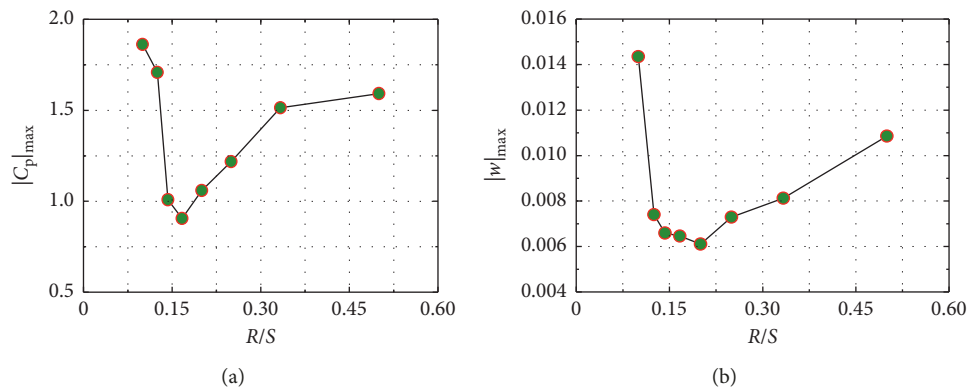


FIGURE 10: Variations of the highest mean suction and the maximum response displacement among all surface nodes with different rise-to-span ratios (R/S). (a) $|C_p|_{\max}$. (b) $|w|_{\max}$.

provides the best performance in reducing wind suction on the roof surface. Figure 12 shows contours of mean pressure coefficients on cylindrical roofs with $R/S = 1/10$, $1/6.25$, and $1/4$. In general, with the increase in the rise-to-span ratio from $1/10$ to $1/4$, the wind suction near the roof apex increases obviously. For the rise-to-span ratio case of $R/S = 1/4$, positive pressure coefficients occur on the windward edge of the roof, with negative pressures over the rest of the structure. However, roof models with $R/S = 1/10$ and $1/6.25$ mainly are dominated by negative pressures.

In order to give a quantitative description of the effects of the rise-to-span ratio on the pressure distribution pattern, Figure 13 compares the mean pressure distributions on the middle transverse cross sections of cylindrical roofs with $R/S = 1/10$, $1/6.25$, and $1/4$. This demonstrates that the highest mean suction near the roof apex has been reduced to 0.87

through the $|C_p|_{\max}$ optimization (optimal $R/S = 1/6.25$). For the roof model with a low rise-to-span ratio ($R/S = 1/10$), extraordinarily large wind suction of $|C_p|_{\max} = 1.77$ can be observed at the leading edge of the windward roof, where strong adverse pressure gradient generates due to the separation of approaching flow. In the case of $R/S = 1/4$, relative large suction ($|C_p|_{\max} = 1.2$) occurs at the roof apex as the rise-to-span ratio increases.

Figure 14 shows the response displacement distributions on single-layer reticulated cylindrical shells subjected to wind loads. It is observed that the maximum displacements of cylindrical shells with $R/S = 1/10$ and $1/4$ appear in the windward region of the roof, with $|w|_{\max} = 0.014$ m and 0.007 m, respectively. However, the maximum displacement for the case of $R/S = 1/6.25$ occurs near the roof apex, and $|w|_{\max} = 0.006$ m. These results

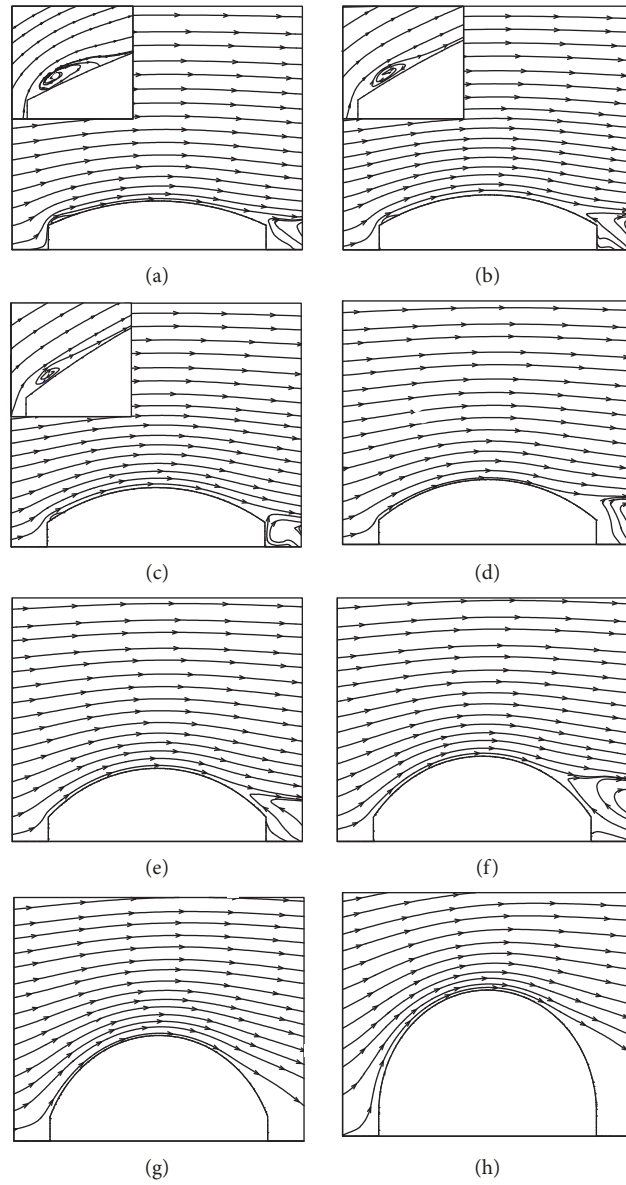


FIGURE 11: Streamline contours around the cylindrical roofs with different rise-to-span ratios. (a) $R/S = 1/10$. (b) $R/S = 1/8$. (c) $R/S = 1/7$. (d) $R/S = 1/6$. (e) $R/S = 1/5$. (f) $R/S = 1/4$. (g) $R/S = 1/3$. (h) $R/S = 1/2$.

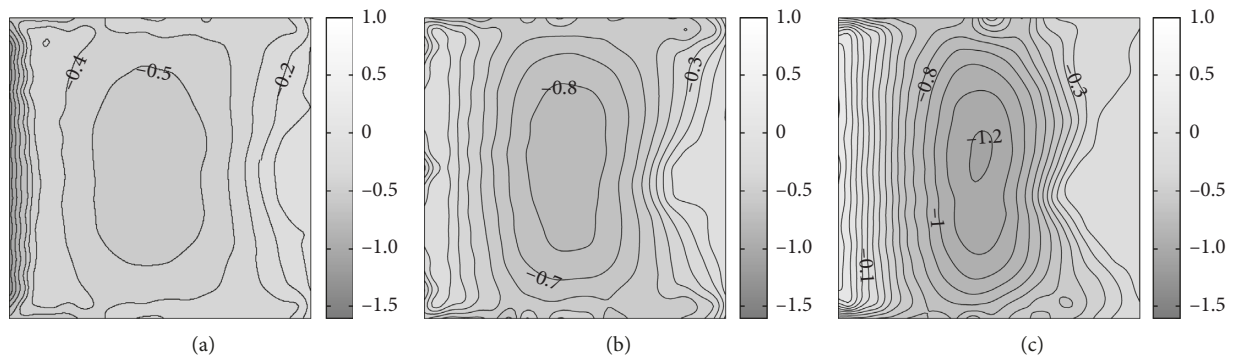


FIGURE 12: Contours of mean pressure coefficients on cylindrical roofs with different rise-to-span ratios. (a) $R/S = 1/10$. (b) $R/S = 1/6.25$. (c) $R/S = 1/4$.

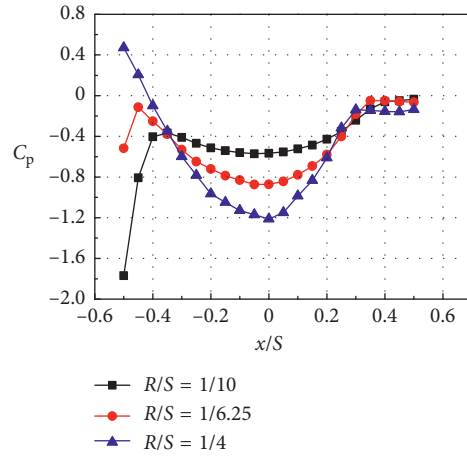


FIGURE 13: Mean pressure distributions on the middle transverse cross sections of cylindrical roofs with different rise-to-span ratios.

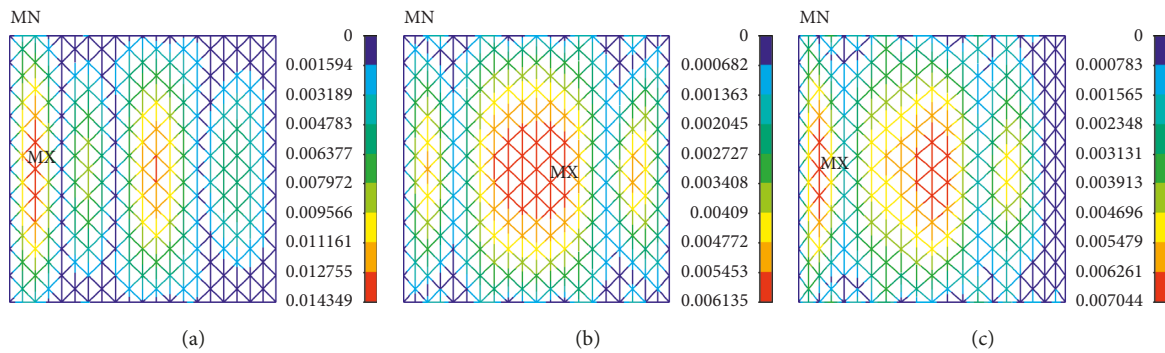


FIGURE 14: The response displacement distributions on single-layer reticulated cylindrical shells with different rise-to-span ratios. (a) $R/S = 1/10$. (b) $R/S = 1/6.25$. (c) $R/S = 1/4$.

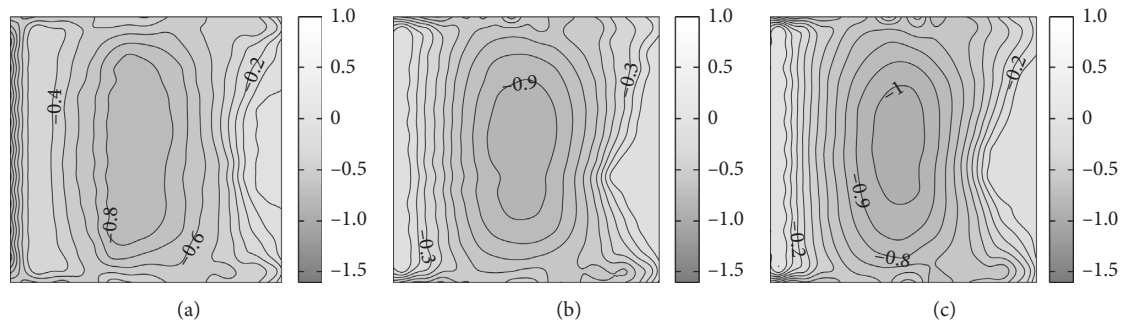


FIGURE 15: Contours of mean pressure coefficients on cylindrical roofs with optimal and near optimal rise-to-span ratios. (a) $R/S = 1/7$. (b) $R/S = 1/5.5$. (c) $R/S = 1/5$.

indicate that the wind-induced displacement of a single-layer reticulated cylindrical shell can be reduced to some extent by applying the highest mean suction optimization.

5.2.2. Maximum Response Displacement Optimization. The optimization procedure (same design variable, constrains, numerical method, etc.) as used in Section 5.2.1 was employed to solve the maximum response displacement

optimization problem. Contours of mean pressure coefficients on cylindrical roofs with optimal and near optimal rise-to-span ratios are shown in Figure 15. The optimal rise-to-span ratio for the $|w|_{\max}$ optimization is 1/5.5. It is found that the overall pressure patterns of the roofs with $R/S = 1/5.5$ and 1/5 are similar, although an increase of wind suction over the roof apex can be observed. Figure 16 shows the mean pressure distributions on the middle transverse cross sections of different models. Note that, in the case of $R/S = 1/$

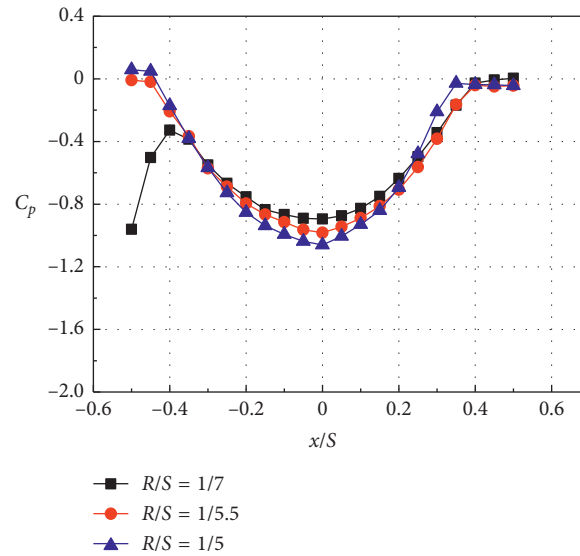


FIGURE 16: Mean pressure distributions on the middle transverse cross sections of cylindrical roofs with optimal and near optimal rise-to-span ratios.

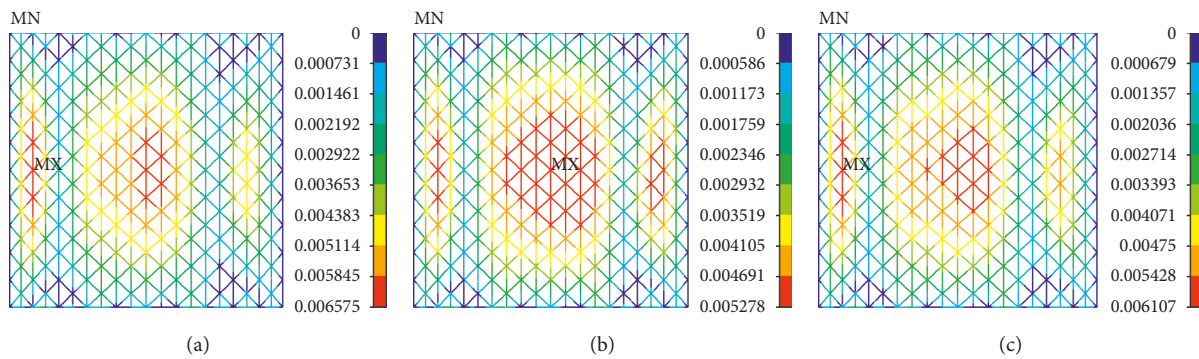


FIGURE 17: The response displacement distributions on single-layer reticulated cylindrical shells with optimal and near optimal rise-to-span ratios. (a) $R/S = 1/7$. (b) $R/S = 1/5.5$. (c) $R/S = 1/5$.

7, relatively large wind suction observed near the leading edge is associated with the flow separation, as shown in Figure 11(c). In general, the $|C_p|_{\max}$ value occurs at the roof apex and slightly increases from 0.90 to 1.06 with R/S ranging from 1/7 to 1/5.

Figure 17 shows the response displacement distributions on single-layer reticulated cylindrical shells with optimal and near optimal rise-to-span ratios. Comparing with the cases of other rise-to-span ratios, as shown in Figures 9 and 14, it can be seen that the wind-induced response of a single-layer reticulated cylindrical shell is particularly sensitive to the variation in the rise-to-span ratio. The results indicate that the maximum displacement occurs near the roof apex and can be reduced to 0.005 m through the $|w|_{\max}$ optimization.

6. Conclusions

This paper proposed an aerodynamic optimization strategy for the identification of an optimal rise-to-span ratio of three-dimensional cylindrical roofs immersed in a shallow turbulent flow. The goals of the optimization were to

minimize the highest mean suction on the roof surface, and the maximum response displacement of a single-layer reticulated cylindrical shell under mean wind loads, respectively. During the optimization procedure, the 3D fluid flow analysis based on RANS equations was performed to evaluate the objective function, and the gradient algorithm was used to find the optimal solution. The contributions obtained from this paper are shown as follows:

- (1) Three-dimensional CFD simulations using four turbulence closure models (standard $k-\epsilon$, RNG $k-\epsilon$, SST $k-\omega$, and RSM) were conducted to investigate the wind load characteristics on cylindrical roofs with different rise-to-span ratios. Each turbulence model results have been compared with the wind tunnel data, and the performance of RSM model is acceptable and is clearly better than other models.
- (2) For the highest mean suction $|C_p|_{\max}$ optimization case, it was found a cylindrical roof with $R/S = 1/6.25$ shows the best performance in attenuating high suction on the roof surface. The $|C_p|_{\max}$ value with

optimal solution is approximately 47% and 55% of the objective values of the initial variables ($R/S = 1/10$ and $1/2$), respectively. For the maximum response displacement $|w|_{\max}$ optimization case, a single-layer reticulated cylindrical shell with $R/S = 1/5.5$ seems to be most effective against mean wind loads, and the $|w|_{\max}$ value can be reduced to approximately 36% and 45% as compared to the cases of $R/S = 1/10$ and $1/2$, respectively. It is important to note that a comparison of the wind load distributions and their effects on single-layer reticulated cylindrical shells with optimal and near optimal solutions has presented a similar trend. Thus, a single-layer reticulated cylindrical shell with R/S in-between $1/6.25$ and $1/5.5$ is considered to be capable of keeping good aerodynamic and mechanical performance.

The main limitations of this research have been the static response analysis under mean wind loads as well as the restricted free-stream flow conditions. A future study will be conducted on the shape optimization of cylindrical roofs with the consideration of dynamic response, under different turbulent flow conditions.

Data Availability

All data used to support the findings of this study are available from the corresponding author upon request.

Conflicts of Interest

The authors declare that there are no conflicts of interest regarding the publication of this paper.

Acknowledgments

This study was financially supported by the National Natural Science Foundation of China under Grant nos. 51808194 and 51578211, the Fundamental Research Funds for the Central Universities under Grant no. 2018B13814, the Natural Science Foundation of Jiangsu Province under Grant no. BK20170880, and the China Postdoctoral Science Foundation under Grant no. 2016M591754.

References

- [1] G. L. Johnson, D. Surry, and W. K. Ng, "Turbulent wind loads on arch-roof structures: a review of model and full-scale results and the effect of Reynolds number," in *Proceedings of the 5th US National Conference on Wind Engineering*, Lubbock, TX, USA, November 1985.
- [2] B. Chen, P. Zhong, W. Cheng, X. Chen, and Q. Yang, "Correlation and combination factors of wind forces on cylindrical roof structures," *International Journal of Structural Stability and Dynamics*, vol. 17, no. 9, article 1750104, 2017.
- [3] J.-H. Chen, "A study on the selection of optimal roof type for low-rise buildings group—in a view of wind pressures action," *Procedia Engineering*, vol. 31, no. 16, pp. 1149–1154, 2012.
- [4] B. Chen and Q. S. Yang, "Effects of geometrical factors on wind pressure characteristics of cylindrical roofs with wind tunnel tests," *Applied Mechanics and Materials*, vol. 351–352, pp. 284–289, 2013.
- [5] P. Huang, X.-Y. Zhou, and M. Gu, "Experimental study of wind loads on cylindrical reticulated shells," *Applied Mathematics and Mechanics*, vol. 34, no. 3, pp. 281–296, 2013.
- [6] Y. Q. Li, Y. Tamura, A. Yoshida, A. Katsumura, and K. Cho, "Wind loading and its effects on single-layer reticulated cylindrical shells," *Journal of Wind Engineering and Industrial Aerodynamics*, vol. 94, no. 12, pp. 949–973, 2006.
- [7] Z. Ding and Y. Tamura, "Contributions of wind-induced overall and local behaviors for internal forces in cladding support components of large-span roof structure," *Journal of Wind Engineering and Industrial Aerodynamics*, vol. 115, pp. 162–172, 2013.
- [8] A. Mistriotis and D. Briassoulis, "Numerical estimation of the internal and external aerodynamic coefficients of a tunnel greenhouse structure with openings," *Computers and Electronics in Agriculture*, vol. 34, no. 1–3, pp. 191–205, 2002.
- [9] R. N. Meroney, C. W. Letchford, and P. P. Sarkar, "Comparison of numerical and wind tunnel simulation of wind loads on smooth, rough and dual domes immersed in a boundary layer," *Wind and Structures*, vol. 5, no. 2–4, pp. 347–358, 2002.
- [10] G. K. Ntinias, X. Shen, Y. Wang, and G. Zhang, "Evaluation of CFD turbulence models for simulating external airflow around varied building roof with wind tunnel experiment," *Building Simulation*, vol. 11, no. 1, pp. 115–123, 2018.
- [11] M. R. Castelli, S. Toniato, and E. Benini, "Numerical analysis of wind loads on a hemicylindrical roof building," *World Academy of Science, Engineering and Technology*, vol. 56, no. 8, pp. 1669–1676, 2011.
- [12] Y. Z. Luo and B. Sun, "Numerical simulation of wind-induced interference between two cylindrical latticed shells in parallel arrangement," *Spatial Structures*, vol. 14, no. 1, pp. 25–31, 2008, in Chinese.
- [13] M. A. Mooneghi and R. Kargarmoakhar, "Aerodynamic mitigation and shape optimization buildings: review," *Journal of Building Engineering*, vol. 6, pp. 225–235, 2016.
- [14] T. Ogawa, M. Ohsaki, T. Miyamura, and T. Kumagai, "Shape optimization of shell roofs subjected to strong wind by using a variable complexity model," *Journal of the International Association for Shell and Spatial Structures*, vol. 46, no. 2, pp. 108–115, 2005.
- [15] T. Yamashita, T. Kumagai, T. Ogawa, T. Miyamura, and M. Ohsaki, "Shape optimization of long-span translational free-form shell roofs in strong wind using multigrid method and variable complexity model," in *Proceedings of the 6th China-Japan-Korea Joint Symposium on Optimization of Structural and Mechanical Systems*, Kyoto, Japan, June 2010.
- [16] E. Bernardini, S. M. J. Spence, D. Wei, and A. Kareem, "Aerodynamic shape optimization of civil structures: a CFD-enabled Kriging-based approach," *Journal of Wind Engineering and Industrial Aerodynamics*, vol. 144, pp. 154–164, 2015.
- [17] A. Elshaer, G. Bitsuamlak, and A. El Damatty, "Enhancing wind performance of tall buildings using corner aerodynamic optimization," *Engineering Structures*, vol. 136, pp. 133–148, 2017.
- [18] V. Yakhot and S. A. Orszag, "Renormalization group analysis of turbulence. I. Basic theory," *Journal of Scientific Computing*, vol. 1, no. 1, pp. 3–51, 1986.
- [19] S. Murakami and A. Mochida, "3-D numerical simulation of airflow around a cubic model by means of the $k-\epsilon$ model,"

- Journal of Wind Engineering and Industrial Aerodynamics*, vol. 31, no. 2-3, pp. 283–303, 1988.
- [20] M. G. Gomes, A. Moret Rodrigues, and P. Mendes, “Experimental and numerical study of wind pressures on irregular-plan shapes,” *Journal of Wind Engineering and Industrial Aerodynamics*, vol. 93, no. 10, pp. 741–756, 2005.
- [21] P. A. C. Rocha, H. H. B. Rocha, F. O. M. Carneiro, M. E. Vieira da Silva, and A. V. Bueno, “ k - ω SST (shear stress transport) turbulence model calibration: a case study on a small scale horizontal axis wind turbine,” *Energy*, vol. 65, pp. 412–418, 2014.
- [22] N. M. Said, H. Mhiri, H. Bournot, and G. Le Palec, “Experimental and numerical modelling of the three-dimensional incompressible flow behaviour in the near wake of circular cylinders,” *Journal of Wind Engineering and Industrial Aerodynamics*, vol. 96, no. 5, pp. 471–502, 2008.
- [23] ANSYS® Academic Research, *ANSYS Fluent User’s Guide Release 15.0*, ANSYS Inc., Canonsburg, PA, USA, 2013.
- [24] C. H. Tsai, J. Kolibal, and M. Li, “The golden section search algorithm for finding a good shape parameter for meshless collocation methods,” *Engineering Analysis with Boundary Elements*, vol. 34, no. 8, pp. 738–746, 2010.
- [25] B. San, Y. Wang, and Y. Qiu, “Numerical simulation and optimization study of the wind flow through a porous fence,” *Environmental Fluid Mechanics*, vol. 18, no. 5, pp. 1057–1075, 2018.
- [26] Y. Qiu, B. San, and Y. Zhao, “Numerical simulation and optimization of wind effects of porous parapets on low-rise buildings with flat roofs,” *Advances in Civil Engineering*, vol. 2019, Article ID 3402613, 11 pages, 2019.



Hindawi

Submit your manuscripts at
www.hindawi.com

